Non-invasive, opsin-free mid-infrared modulation activates cortical neurons and accelerates associative learning

Xiaowei Chen (xiaowei_chen@tmmu.edu.cn)
Third Military Medical University https://orcid.org/0000-0003-0906-6666
Jianxiong Zhang
Third Military Medical University
Yong He
National Innovation Institute of Defense Technology
Shanshan Liang
Third Military Medical University
Xiang Liao
Third Military Medical University https://orcid.org/0000-0001-6324-5206
Tong Li
Third Military Medical University
Zhi Qiao
National Innovation Institute of Defense Technology
Chao Chang
National Innovation Institute of Defense Technology
Hongbo Jia
Suzhou Institute of Biomedical Engineering and Technology, Chinese Academy of Sciences
https://orcid.org/0000-0003-1585-2161

Article

Keywords: stimulation technique, mid-infrared modulation (MIM), non-invasive, opsin-free, brain learning capability

Posted Date: September 9th, 2020

DOI: https://doi.org/10.21203/rs.3.rs-70564/v1

Version of Record: A version of this preprint was published at Nature Communications on May 12th, 2021. See the published version at https://doi.org/10.1038/s41467-021-23025-y.

Abstract

Boosting learning capability represents a long-sought dream of mankind. Neurostimulant drugs or magnetic/electrical stimulation techniques can overcome attention deficits, but these drugs or techniques are weakly beneficial in boosting the learning capabilities of healthy subjects. Here, we report a stimulation technique, mid-infrared modulation (MIM), that delivers mid-infrared light energy through opened skull or even non-invasively through thinned intact skull and can activate brain neurons in vivo without introducing any exogeneous gene. Using c-Fos immunohistochemistry, in vivo single-cell electrophysiology and two-photon Ca^{2+} imaging in mice, we demonstrate that MIM significantly induces firing activities of neurons in the targeted cortical area. Moreover, mice that receive MIM targeting to the auditory cortex during an auditory associative learning task exhibit a strikingly faster learning speed (~ 50% faster) than control mice. Together, this non-invasive, opsin-free MIM technique is demonstrated with a great translational potential for activating brain neurons and boosting brain learning capability.

Main

It has become increasingly popular for people to take some neurostimulant drugs as nootropics[1] that are expected to enhance cognition and learning[2] beyond the initially approved therapeutic purposes such as curing attention deficits[3]. Likewise, brain stimulation techniques, including, e.g., transcranial magnetic stimulation[4] and transcranial direct-current stimulation[5], have also been extensively practiced in healthy subjects with similar expectations. However, while those drugs or stimulation techniques could help alleviating the relevant deficits, their resulting effects in the diseased conditions do not necessarily imply that healthy subjects could benefit from them in boosting the normal learning capabilities.

Learning is an intricate process that involves highly specific patterns of neuronal activation[6–8], and the neocortex is known to be functionally relevant for the associative learning process[9–11]. In the past decade, specific manipulations of neuronal activities have been achieved by using the optogenetic technique[12], advancing the understanding of learning and memory formation[13]. Although having become highly popular for animal experiments, the optogenetics technique shows little potential for applications in healthy humans due to the requirement of introducing exogenous genes in the brain. Here, we present a fundamentally different energy stimulation technique, mid-infrared modulation (MIM), which delivers mid-infrared light (MIR) energy through opened skull or even non-invasively through thinned intact skull to the brain and can significantly elevate neuronal firing rates in the targeted brain region. Notably, MIM induces neuronal firing in complete absence of any exogeneous gene. As a striking example, we demonstrate that MIM application in the auditory cortex of healthy adult mice during a sound-licking associative learning task boosts learning speed by ~ 50%.

We used a pulsed quantum cascade laser as the MIR light source for MIM in this study (see Supplemental Methods for details). A MIR fiber (core diameter 100 μm, numerical aperture 0.27) delivered the MIR to the target region of mouse brain (Fig. 1a), in a manner superficially similar to fiber-based

optogenetics technique[14]. However, two major features fundamentally distinguish MIM from optogenetics. First, no exogeneous gene was introduced into the brain. Second, the wavelength of stimulation light was 5.6 μm, which is in the mid-infrared spectrum (3–50 μm, as defined by the ISO 20473 standard) and far beyond the visible (VIS, 0.38–0.78 μm) to near-infrared (NIR, 0.78–3 μm) spectrum used in optogenetics[14].

We delivered the MIR with the following parameters: average irradiation power 9 ± 0.5 mW (5 measurements at the fiber tip), pulse width 300 ns, repetition rate 100 kHz, and irradiation duration 20 s (for detailed protocol, see Supplemental Methods). In order to yield repeatable and comparable results, we first placed the fiber tip closely above the cortical surface following craniotomy. After MIR delivery we performed immunohistochemistry for c-Fos (see Supplemental Methods), a widely-used molecular marker of neuronal activation[15]. C-Fos positive cells were found in a bullethead-shaped volume that was mostly within layer 2/3 of the cortex (Fig. 1b), where the axial and lateral extent of the distribution was both ~ 400 μm (Fig. 1c). Within this zone (e.g., outlined in Fig. 1b), the proportion of c-Fos positive cells among all cells was 27.8 / 24.0–32.1% (n = 21 slices from 7 animals, median / 1st – 3rd quartile, same notation for all subsequent data if not stated otherwise).

We next performed a dose-dependent test and found that the c-Fos cell count positively correlated with the irradiation time in our tested range between 5 s and 60 s (Fig. 1d, left 4 columns, c-Fos positive cell count per slice image, '5 s': 16 / 11.75–23, n = 11; '10 s': 38 / 19.75–45, n = 9; '20 s': 46.5 / 39.5–63, n = 12; '60 s': 165 / 130–188, n = 14). Having shown that MIM application through opened skull could reliably induce neuronal activation, we applied MIM to the mice with thinned intact skull (thickness remaining: 44 / 37–48 μm, n = 12 measurements). MIM through thinned intact skull (irradiation time of 20 s) also induced neuronal activation (Fig. 1d, 'Thinned 20 s', c-Fos cell count: 24.5 / 19–42, n = 8). Comparing to the dose-dependent test, we estimate that the neuronal activation efficiency through thinned intact skull is about half (52%) of that through opened skull.

We conducted a new set of experiments wherein MIR and VIS light were delivered to each side of the cortex of individual mice respectively (both through opened skull, Fig. 1e), each via a fiber with the same geometric parameters and with the same irradiation power (9 mW) and time (20 s). Copious c-Fos positive cells were present in the MIR- but not the VIS-targeted regions (Fig. 1f). A few c-Fos positive cells were found at superficial locations within 70 μm from the cortical surface (*i.e.*, layer 1); cells here are generally not considered to be pyramidal neurons[16]. Thus, we re-calculated the c-Fos positive cell count for this experiment by excluding these labeled superficial cells, and found that the count in the VIS region was near zero (Fig. 1g, MIR: 45.5 / 42–68, n = 8 slices from 4 animals; VIS: 1.5 / 1–3, n = 13 slices from 4 animals, p = 1e-4, rank sum test).

How does MIR light activate neurons without opsins? This activation was unlikely due to general heating, because previous studies have shown that heating (up to 2°C) by VIS light at a comparable power level (*e.g.*, 15 mW in their studies versus the 9 mW of MIR in our study) either does not change or even suppresses neuronal activities through activation of an inwardly rectifying potassium conductance[17,18].

Furthermore, other studies have reported that pulsed NIR light induces neuronal activation not by general heating, but rather by a transient spatiotemporal gradient of light energy absorption in the tissue[19,20]. The higher water absorption coefficient for MIR relative to VIS or NIR light[21] could be advantageous for efficiently establishing such gradients in a confined volume of brain tissue (see Fig. 1b, c for the spatial confinement). Such transient gradients may account for the efficiency of MIR energy to activate neurons without opsins. Moreover, the MIR light could induce conformational changes in particular proteins via nonlinear molecular resonance absorption[22], further supporting the potential utility of MIR energies for modulating neuronal excitability and inducing firing activities.

To demonstrate that MIM could indeed induce neuronal firing, we performed *in vivo* single-cell loose-patch recording in cortical neurons throughout a course of MIM application (Fig. 1h). Figure 1i shows an example neuron that exhibited a greatly elevated firing rate in the MIM time window (across three consecutive trials). A summary of 5 recorded neurons (out of 9 loose-patched neurons) shows a significant elevation in the firing rate in the MIM window as compared to that in the pre- or post- MIM windows (Fig. 1j). These experiments above together establish a basic proof-of-principle for MIM *in vivo*, demonstrating that MIR energy delivery indeed induces neuronal firing in absence of any exogeneous gene.

We next employed two-photon Ca^{2+} imaging[23–25] to visualize live neuronal population activities during MIM application (Fig. 2a, see also Supplemental Methods). Auditory cortical neurons were labeled with a Ca^{2+}-sensitive fluorescent dye, Cal-520 (e.g., Fig. 2b). We performed real-time (40 Hz) two-photon imaging over the entire course of MIM application (40 s before, 20 s MIR irradiation, 60 s after). An example neuron (Fig. 2c) showed that MIM application reliably induced Ca^{2+} transients during the application time window over repeated trials. For each animal, we sequentially performed real-time imaging recordings (as the example above) at multiple cortical depths, which enabled mapping of the MIM-activated neurons (e.g., Fig. 2d). Note that a neuron was defined as MIM-activated if its trial-averaged Ca^{2+} activity level during the MIM window exceeded the activity level detected for the baseline window (before the irradiation window) by more than 2-fold (see Supplemental Methods).

Out of a total of 1532 neurons from 6 animals, we found 167 MIM-activated neurons (Fig. 2e, for the complete dataset see extended data Fig. 1). The activity level for the MIM-activated neurons recovered after the MIM window, returning to the same level as before irradiation (see also the average Ca^{2+} signal trace in Fig. 2e). Note that the proportion of MIM-activated neurons detected in these two-photon Ca^{2+} imaging experiments was 10.2 / 4.0–17.5% (n = 26 imaging focal planes from 6 animals), which was lower than that in the c-Fos imaging results (27.8 / 24.1–32.1%, n = 21 slices from 7 animals). We speculate that this difference could result from methodological differences, *i.e.*, c-Fos imaging captures the cumulative neuronal activities from a prolonged time (the time required for c-Fos expression[15] is much longer than the neuronal activation time), whereas two-photon Ca^{2+} imaging resolves specific neuronal activities in real time. Nevertheless, our results from c-Fos imaging, two-photon Ca^{2+} imaging,

and single-cell loose-patch recording are highly consistent in demonstrating that MIM activates a substantial number of neurons in the targeted cortical region.

Previous studies have reported that the activities of auditory cortical neurons are involved in auditory associative learning for mice[9,10,26]. We therefore tested whether and how MIM application in the auditory cortex might affect the learning course for a sound-licking associative learning task[24] (Fig. 3a). We recruited three cohort groups of naïve, healthy mice (8–9 weeks old at the beginning of training): the 'control' group that did not receive any MIM application, the 'MIM-opened' group that received MIM application through opened skull (a small craniotomy of ~ 200 μm diameter over the auditory cortex) and the 'MIM-thinned' group that received MIM application through thinned intact skull. All groups went through the same training program (consisting of 6 sessions). From session #2 on, animals in the two MIM groups received MIM application during the task engagement time windows (Fig. 3b, 25–35 s per engagement window with a 60 s pause between each). A typical example of a behavioral recording over consecutive trials during the learning process is shown in Fig. 3c, in which there were three successful response events (licking initiated within 0.5 s after sound stimulus onset) and one missed event (either no licking or licking initiated later than 0.5 s after sound).

The result showed that the licking action latency of successful response event became slightly shorter with increasing training sessions for all groups; however, no significant difference in the response latency among any pair of groups was found in any session (Fig. 3d). On the other hand, starting at the same level of response success rate in session #1 (Fig. 3e, success rate in session #1, 'control' group: 28.5 / 19.7–33.4%, $n = 13$; comparing to: 'MIM-opened' group: 25.9 / 17.9–38.2%, $n = 14$; $p = 0.96$; 'MIM-thinned' group: 18.5 / 8.2–35.4%, $n = 8$; $p = 0.32$; rank sum test), both the 'MIM-opened' and the 'MIM-thinned' groups achieved a significantly more increment in the response success rate over the first half of the learning course (Fig. 3e, increment of success rate from session #1 to session #3, 'control' group: 26.8 / 22.6–33.1%, $n = 13$; comparing to: 'MIM-opened' group: 40.5 / 30.4–57.8%, $n = 14$; $p = 0.027$; 'MIM-thinned' group: 50 / 37.8–57.1%, $n = 8$; $p = 0.031$; rank sum test). These results together suggest that MIM does not affect the behavioral action latency, but rather boosts the sensory-behavior associative learning speed.

We fitted a learning curve for each mouse (Fig. 3f shows the group average) using an exponential function[27], and then defined the learning speed by the fitted exponent factor. Comparing to the 'control' group, MIM boosted learning speed by ~ 50% for either group with thinned intact skull or opened skull (Fig. 3g, fitted exponent factor, 'control' group: 0.29 / 0.25–0.33, $n = 13$; 'MIM-opened' group: 0.44 / 0.38–0.51, $n = 14$; $p = 0.004$; 'MIM-thinned' group: 0.45 / 0.32–0.54, $n = 8$; $p = 0.03$; rank sum test). Note that in this set of associative learning experiments we applied MIM repeatedly over multiple trials (Fig. 3b). Thus, the reduced neuronal activation efficiency through thinned intact skull obtained by the c-Fos imaging experiments with a single-shot MIM (Fig. 1d) is not incompatible with the result here that, MIM through thinned intact skull achieved nearly the same degree of learning acceleration as that of MIM through opened skull.

Associative learning is generally assumed to require synaptic plasticity, which in mammals is known to depend on the temporal coincidence of synaptic and somatic activities[28–30]. Thus, we speculate that the observed acceleration of sensory-behavior associative learning likely results from extra MIM-induced somatic activities (Fig. 2) that coincide temporally with the task-relevant synaptic input activities occurring during the engagement window. In this scenario, the increase in coincident synaptic and somatic activities would result in an overall increase in the amount of task-relevant synaptic plasticity during a given task engagement duration, thus accelerating the learning. From another viewpoint[31], the MIM-induced activation of a subset of cortical neurons (Fig. 1, 2) during the learning task could promote the recruitment of these neurons into the engram cell population[32], thus accelerating the learning.

In this study, we demonstrate MIM, a non-invasive and opsin-free neuronal stimulation technique that is fundamentally different from the well-known and widely-deployed optogenetics technique[12,14]. MIM reliably induces neuronal activations in a precisely targeted and spatially confined volume of brain tissue *in vivo*, in a manner similar to that of optogenetics but in complete absence of introducing exogeneous gene. Like that optogenetics application is shown to artificially alter memory, sensory perception or behavior control[33,34], we show here that MIM application in the auditory cortex profoundly accelerates the sound-licking associative learning (Fig. 3e, g). Together, our results illustrate the utility of this promising technique for enhancing brain learning functions with mid-infrared light energy.

Declarations

Competing interests

The authors declare no competing interests.

References

1. Sahakian, B. & Morein-Zamir, S. Professor's little helper. *Nature* 450, 1157–1159, (2007).
2. Kortekaas-Rijlaarsdam, A. F., Luman, M., Sonuga-Barke, E. & Oosterlaan, J. Does methylphenidate improve academic performance? A systematic review and meta-analysis. *European Child & Adolescent Psychiatry* 28, 155–164, (2019).
3. Lange, K. W., Reichl, S., Lange, K. M., Tucha, L. & Tucha, O. The history of attention deficit hyperactivity disorder. *Attention deficit and hyperactivity disorders* 2, 241–255, (2010).
4. Lefaucheur, J. P. *et al.* Evidence-based guidelines on the therapeutic use of repetitive transcranial magnetic stimulation (rTMS). *Clinical neurophysiology* 125, 2150–2206, (2014).
5. Lefaucheur, J. P. *et al.* Evidence-based guidelines on the therapeutic use of transcranial direct current stimulation (tDCS). *Clinical neurophysiology* 128, 56–92, (2017).
6. Zhu, Y. *et al.* Dynamic salience processing in paraventricular thalamus gates associative learning. *Science* 362, 423–429, (2018).

7. Josselyn, S. A. & Tonegawa, S. Memory engrams: Recalling the past and imagining the future. *Science* 367, (2020).
8. Poo, M. M. *et al.* What is memory? The present state of the engram. *BMC biology* 14, 40, (2016).
9. Dalmay, T. *et al.* A Critical Role for Neocortical Processing of Threat Memory. *Neuron* 104, 1180–1194.e1187, (2019).
10. Letzkus, J. J. *et al.* A disinhibitory microcircuit for associative fear learning in the auditory cortex. *Nature* 480, 331–335, (2011).
11. Aschauer, D. & Rumpel, S. The Sensory Neocortex and Associative Memory. *Current topics in behavioral neurosciences* 37, 177–211, (2018).
12. Boyden, E. S., Zhang, F., Bamberg, E., Nagel, G. & Deisseroth, K. Millisecond-timescale, genetically targeted optical control of neural activity. *Nature neuroscience* 8, 1263–1268, (2005).
13. Liu, X. *et al.* Optogenetic stimulation of a hippocampal engram activates fear memory recall. *Nature* 484, 381–385, (2012).
14. Zhang, F. *et al.* Optogenetic interrogation of neural circuits: technology for probing mammalian brain structures. *Nature protocols* 5, 439–456, (2010).
15. Krukoff, T. L. in *Cell Neurobiology Techniques* (eds Alan A. Boulton, Glen B. Baker, & Alan N. Bateson) 213–230 (Humana Press, 1999).
16. Lee, A. J. *et al.* Canonical Organization of Layer 1 Neuron-Led Cortical Inhibitory and Disinhibitory Interneuronal Circuits. *Cerebral cortex* 25, 2114–2126, (2015).
17. Owen, S. F., Liu, M. H. & Kreitzer, A. C. Thermal constraints on in vivo optogenetic manipulations. *Nature Neuroscience* 22, 1061–1065, (2019).
18. Ait Ouares, K., Beurrier, C., Canepari, M., Laverne, G. & Kuczewski, N. Opto nongenetics inhibition of neuronal firing. *The European journal of neuroscience* 49, 6–26, (2019).
19. Thompson, A. C., Stoddart, P. R. & Jansen, E. D. Optical Stimulation of Neurons. *Current molecular imaging* 3, 162–177, (2014).
20. Rajguru, S. M. *et al.* Infrared photostimulation of the crista ampullaris. *J Physiol* 589, 1283–1294, (2011).
21. Afsah-Hejri, L., Hajeb, P., Ara, P. & Ehsani, R. J. A Comprehensive Review on Food Applications of Terahertz Spectroscopy and Imaging. *Comprehensive Reviews in Food Science and Food Safety* 18, 1563–1621, (2019).
22. Son, J. H. *Terahertz Biomedical Science and Technology*. (CRC Press, 2014).
23. Tischbirek, C. H. *et al.* In Vivo Functional Mapping of a Cortical Column at Single-Neuron Resolution. *Cell Rep* 27, 1319–1326 e1315, (2019).
24. Li, R. *et al.* Two-Photon Functional Imaging of the Auditory Cortex in Behaving Mice: From Neural Networks to Single Spines. *Front Neural Circuits* 12, 33, (2018).
25. Rothschild, G., Nelken, I. & Mizrahi, A. Functional organization and population dynamics in the mouse primary auditory cortex. *Nature neuroscience* 13, 353–360, (2010).

26. Li, J. C. *et al.* Primary Auditory Cortex is Required for Anticipatory Motor Response. *Cerebral Cortex* 27, 3254–3271, (2017).
27. Leibowitz, N., Baum, B., Enden, G. & Karniel, A. The exponential learning equation as a function of successful trials results in sigmoid performance. *Journal of Mathematical Psychology* 54, 338–340, (2010).
28. Dan, Y. & Poo, M. M. Spike timing-dependent plasticity of neural circuits. *Neuron* 44, 23–30, (2004).
29. Bi, G.-q. & Poo, M.-m. Synaptic Modification by Correlated Activity: Hebb's Postulate Revisited. *Annual Review of Neuroscience* 24, 139–166, (2001).
30. Markram, H., Lübke, J., Frotscher, M. & Sakmann, B. Regulation of synaptic efficacy by coincidence of postsynaptic APs and EPSPs. *Science* 275, 213–215, (1997).
31. Titley, H. K., Brunel, N. & Hansel, C. Toward a Neurocentric View of Learning. *Neuron* 95, 19–32, (2017).
32. Kitamura, T. *et al.* Engrams and circuits crucial for systems consolidation of a memory. *Science* 356, 73–78, (2017).
33. Zhou, T. *et al.* History of winning remodels thalamo-PFC circuit to reinforce social dominance. *Science* 357, 162–168, (2017).
34. Lee, S. H. *et al.* Activation of specific interneurons improves V1 feature selectivity and visual perception. *Nature* 488, 379–383, (2012).

Methods

Animals

C57BL/6J male mice (2-3 months old) were provided by the Laboratory Animal Center of the Third Military Medical University. All experimental procedures were performed in accordance with institutional animal welfare guidelines with the approval of the Third Military Medical University Animal Care and Use Committee.

Mid-infrared light source

A quantum cascade mid-infrared (MIR) laser (Daylight solution Inc., Model ‘MIRcat’) was used for this study. The laser contains four modules for continuous wavelength tuning but it was set to work constantly at 5.6 μm wavelength for this study. The output was coupled with a MIR fiber (IRF-Se-100, Label No. 11822-01) with a core diameter of 100 μm and a numerical aperture (NA) of 0.27. For all experiments in this study, the average power at the fiber tip (measured in the air) was at a stable level of 9 ± 0.5 mW with the following configurations: pulse duration 300 ns, repetition rate 100 kHz, pump current 650 mA, and duty cycle 3%.

Immunohistochemistry

For the c-Fos experiments (Fig. 1), the animal was first head-fixed under general anesthesia with isoflurane (1.5%). The fiber tip was placed either above the brain surface via an open craniotomy or over the thinned intact skull (Fig. 1d). After the MIM application, the animal was kept under anesthesia for 90 minutes for c-Fos expression. The animal was then transcardially perfused with 4% paraformaldehyde (PFA) and the brain was fixed in 15% sucrose in 4% PFA and refrigerated overnight at 4°C. Coronal sections (thickness: 44 μm) encompassing the fiber target spot were made by a vibratome. The c-Fos immunostaining was performed with the primary antibody: Anti-c-Fos (ABE457, Millipore), followed by the secondary antibody: Alexa Fluor 594 goat anti-rabbit 1:500 (A11012, Molecular Probes). DAPI (4', 6-diamidino-2-phenylindole, D9564, Sigma-Aldrich) was used to stain cell nuclei (1:10000 dilution). Sections were mounted on slides with coverslips and imaged using a scanning confocal microscope (TCS SP5, Leica).

Loose-patch recording

For loose-patch recordings in cortical neurons *in vivo*, we used the 'shadow-patching' procedure according to previous studies[1-4], except that we did not rupture the membrane of targeted cells to maintain a loose-patch configuration. Cell-attached recordings were performed with an *EPC10* amplifier (HEKA Elektronik, Germany). The glass electrode filled with normal ACSF had a tip resistance of 5-8 MΩ. Raw signals were filtered at 10 kHz and sampled at 20 kHz using *Patchmaster* software (HEKA Elektronik, Germany).

Two-photon Ca^{2+} imaging

For the acute two-photon Ca^{2+} imaging experiments (Fig. 2), we exposed the right auditory cortex of the mouse, as described in previous studies[2,5]. The animal was anaesthetized by isoflurane and kept on a warm plate (37.5°C). The skin and muscles over the auditory cortex were removed after local lidocaine injection. A custom-made plastic chamber was glued to the skull with cyanoacrylate glue (UHU), followed by a small craniotomy (~2 mm × 2 mm) (the centre point: Bregma -3.0 mm, 4.5 mm lateral to midline). These stereotaxic coordinates correspond to a larger region of the auditory cortex, including the primary auditory cortex (Au1), the dorsal and ventral secondary auditory cortex (AuD and AuV) as well as a part of the adjacent temporal association cortex (TeA)[6]. After performing the craniotomy, the animal was transferred to the imaging rig with a head-fixation chamber. The chamber was perfused with normal artificial cerebral spinal fluid (ACSF) containing 125 mM NaCl, 4.5 mM KCl, 26 mM $NaHCO_3$, 1.25 mM NaH_2PO_4, 2 mM $CaCl_2$, 1 mM $MgCl_2$ and 20 mM glucose (pH 7.4 when bubbled with 95% oxygen and 5% CO_2). The Ca^{2+} dye, Cal-520 AM (AAT Bioquest), was dissolved in DMSO with 20% Pluronic F-127 to a final concentration of 567 μM for bolus loading. The loading procedure was the same as that in previous literature[7-9], by means of pressured injection via a micropipette inserted in the cortex. About 2 hours after dye injection to allow sufficient cellular uptake, two-photon imaging was performed with a custom-built two-photon microscope system based on a 12.0 kHz resonant scanner (model "LotosScan 1.0", Suzhou Institute of Biomedical Engineering and Technology[10,11]). Two-photon excitation light was delivered by a mode-locked Ti:Sa laser (model "Mai-Tai DeepSee", Spectra Physics) at a near-infrared (NIR) wavelength

of 920 nm. A 40X/0.8 NA (Nikon) water-immersion objective was used for imaging, and this objective had a long working distance of 3.5 mm and a large access angle of ~40 degree to allow micropipette manipulations from the side. We placed the fiber tip from an oblique angle to the cortical surface and protected it by a glass micropipette to avoid excess contact with ACSF. The typical size of the imaging field-of-view (FOV) was ~ 200 μm x 200 μm. In a typical experiment, time-lapse imaging recording at different focal depths could be performed sequentially. The average power of the imaging laser (under the objective) was in the range of 30 to 120 mW, depending on the depth of imaging.

Associative training

For the sound-licking associative training experiments (Fig. 3) we adapted the training protocol as described in previous studies[2,8,12]. Sound stimuli were delivered by an ED1 electrostatic speaker driver and a free-field ES1 speaker (both from Tucker Davis Technologies). The distance from the speaker to the mouse ear (contralateral to the imaged A1) was ~6 cm. The sound stimulus was produced by a custom-written, LabVIEW-based program (LabVIEW 2012, National Instruments) and transformed to analogue voltage through a PCI6731 card (National Instruments). Sound levels tested with a microphone placed ~6 cm away from the speaker were calibrated by a pre-polarized condenser microphone (377A01 microphone, PCB Piezotronics Inc.). For broadband noise (BBN, bandwidth 0-50 kHz), the sound level was ~65 dB sound pressure level (SPL). A waveform segment of BBN was first generated, and the same waveform segment was used for all experiments (i.e., a 'frozen noise'). The duration of a sound stimulus was 50 ms.

Before training, the animal was implanted with the headpost under isoflurane anaesthesia and then allowed to recover for 5 days. For animals in 'MIM-opened' or 'MIM-thinned' group, the fiber tip was fixed above the cortical surface or the thinned section of skull, respectively, before the beginning of each session from session #2 on (and was removed after the end of session). The stereotaxic coordinates used for the placement of the fiber tip were the same as those for two-photon Ca^{2+} imaging experiments in the auditory cortex. Careful management of water consumption was taken to ensure that animals in all groups received similar volume of water and had a similar level of motivation throughout all sessions and days. During the training sessions, the animal was head-fixed to the training rig. A droplet of water was formed at a spout by automatically controlled pumping (pumping duration, 20 ms) at 100 ms after the end of the sound stimulus (in total, 50 + 100 = 150 ms from the stimulus onset). Water droplets remained at the spout after being delivered so that the animal could always obtain water if ever it voluntarily made a licking action at any time after water was delivered. If the animal had not licked before the next trial occurred, a new droplet would replace the previous one at the spout. The spout was positioned at a distance of approximately 3–4 mm from the animal mouth (and with no visible ambient light) such that the animal had to voluntarily stretch out its tongue to probe and acquire water droplets on the spout. Licking actions were monitored by a camera (frame rate 30 Hz) under NIR illumination that was invisible to the animals. There was no cue, stimulus or rewarding/punishing object beyond the sound and the water. We did not apply any punishment for incorrect licking timing.

One training session contained 100 sound stimulation events. These stimuli were delivered in 25 discrete engagement time windows, each consisting of 4 events with random inter-trial intervals (in the range of 5 – 10 s, longer than the duration of a licking action). The rationale of using a randomized inter-trial interval setting was to avoid the possible effect of the rhythmic predicative responses that have been known to exist in mice[12]. Each engagement time window was followed by a 60-s pause with neither sound nor water being present. For animals in MIM group, the MIR irradiation was turned on (by a sound-free electronic shutter) during the engagement time window (which was 20 – 35 s depending on the random inter-trial interval, similar to the MIM applications in the two-photon imaging experiments).

A success sound-evoked licking event was defined as an event in which the animal initiated a licking action within 500 ms from sound stimulus onset, otherwise the event was defined as a miss. For a session, the success rate was defined as the number of success events divided by the total number of events. For analysing the licking response latency, the behavior monitoring videos were first inspected by humans and the video frame of licking action onset was marked for each trial. The response latency was then defined as the duration from the sound stimulation onset to the first video frame in which the animal stretched out its tongue (as shown in Fig. 3c right).

Ca^{2+} imaging data analysis

We analysed our data using custom-written software in LabVIEW 2012 (National Instruments), Igor Pro 5.0 (Wavemetrics) and MATLAB 2014a (MathWorks), as previously published[13]. To correct motion-related artefacts in imaging data, we used a frame-by-frame alignment algorithm to minimize the sum of squared intensity differences between each frame image and a template, which is the average of the selected image frames.

To extract fluorescence signals, we visually identified neurons and performed the drawing of regions of interest (ROIs) based on fluorescence intensity. Fluorescence changes (f) were calculated by averaging the corresponding pixel values in each specified ROI. Relative fluorescence changes $\Delta f/f = (f-f_0)/f_0$ were calculated as Ca^{2+} signals, where the baseline fluorescence f_0 was estimated as the 25th percentile of the entire fluorescence recording. Glial cells were excluded from our analysis according to morphology and Ca^{2+} transient time course.

As described in our previous studies[12,14], we performed automatic Ca^{2+} transient detection based on thresholding criteria regarding peak amplitude and rising rate, which is similar to the peeling approaches previously described by the Helmchen laboratory[15]. During the licking task, licking activities were semi-automatically tracked from the monitoring movie and quantified as a time course, as described previously[8,12].

Statistical tests

To compare data between groups, we used non-parametric Wilcoxon rank sum test (unpaired) to determine statistical significance between them. In the text, summarized data are presented as the median/25^{th} – 75^{th} percentiles. In the figures, the data presented in the box-and-whisker plots indicate the median (centre line), 25%-75% IQR (box), minimum and maximum (whiskers). We used Matlab 2014a to generate the boxplots, for which, the software automatically excluded outlier datapoints for plotting the whiskers ("An observation is defined as an outlier if it falls more than 1.5 × IQR above the third quartile or below the first quartile.").

Methods References

1. Chen, X. *et al.* Disruption of the olivo-cerebellar circuit by Purkinje neuron-specific ablation of BK channels. *Proc Natl Acad Sci U S A* 107, 12323-12328, (2010).
2. Chen, X., Leischner, U., Rochefort, N. L., Nelken, I. & Konnerth, A. Functional mapping of single spines in cortical neurons in vivo. *Nature* 475, 501-505, (2011).
3. Chen, X. *et al.* LOTOS-based two-photon calcium imaging of dendritic spines in vivo. *Nature protocols* 7, 1818-1829, (2012).
4. Chen, X., Rochefort, N. L., Sakmann, B. & Konnerth, A. Reactivation of the same synapses during spontaneous up states and sensory stimuli. *Cell Rep* 4, 31-39, (2013).
5. Rothschild, G., Nelken, I. & Mizrahi, A. Functional organization and population dynamics in the mouse primary auditory cortex. *Nature neuroscience* 13, 353-360, (2010).
6. Dalmay, T. *et al.* A Critical Role for Neocortical Processing of Threat Memory. *Neuron* 104, 1180-1194.e1187, (2019).
7. Stosiek, C., Garaschuk, O., Holthoff, K. & Konnerth, A. In vivo two-photon calcium imaging of neuronal networks. *Proc Natl Acad Sci U S A* 100, 7319-7324, (2003).
8. Li, R. *et al.* Two-Photon Functional Imaging of the Auditory Cortex in Behaving Mice: From Neural Networks to Single Spines. *Front Neural Circuits* 12, 33, (2018).
9. Tischbirek, C. H. *et al.* In Vivo Functional Mapping of a Cortical Column at Single-Neuron Resolution. *Cell Rep* 27, 1319-1326 e1315, (2019).
10. Jia, H., Rochefort, N. L., Chen, X. & Konnerth, A. Dendritic organization of sensory input to cortical neurons in vivo. *Nature* 464, 1307-1312, (2010).
11. Jia, H., Varga, Z., Sakmann, B. & Konnerth, A. Linear integration of spine Ca2+ signals in layer 4 cortical neurons in vivo. *Proc Natl Acad Sci U S A* 111, 9277-9282, (2014).
12. Li, J. C. *et al.* Primary Auditory Cortex is Required for Anticipatory Motor Response. *Cerebral Cortex* 27, 3254-3271, (2017).
13. Guan, J. H. *et al.* NeuroSeg: automated cell detection and segmentation for in vivo two-photon Ca2+ imaging data. *Brain Struct. Funct.* 223, 519-533, (2018).
14. Li, J. *et al.* Functional imaging of neuronal activity of auditory cortex by using Cal-520 in anesthetized and awake mice. *Biomedical optics express* 8, 2599-2610, (2017).

15. Grewe, B. F., Langer, D., Kasper, H., Kampa, B. M. & Helmchen, F. High-speed in vivo calcium imaging reveals neuronal network activity with near-millisecond precision. *Nature methods* 7, 399-405, (2010).

Figures

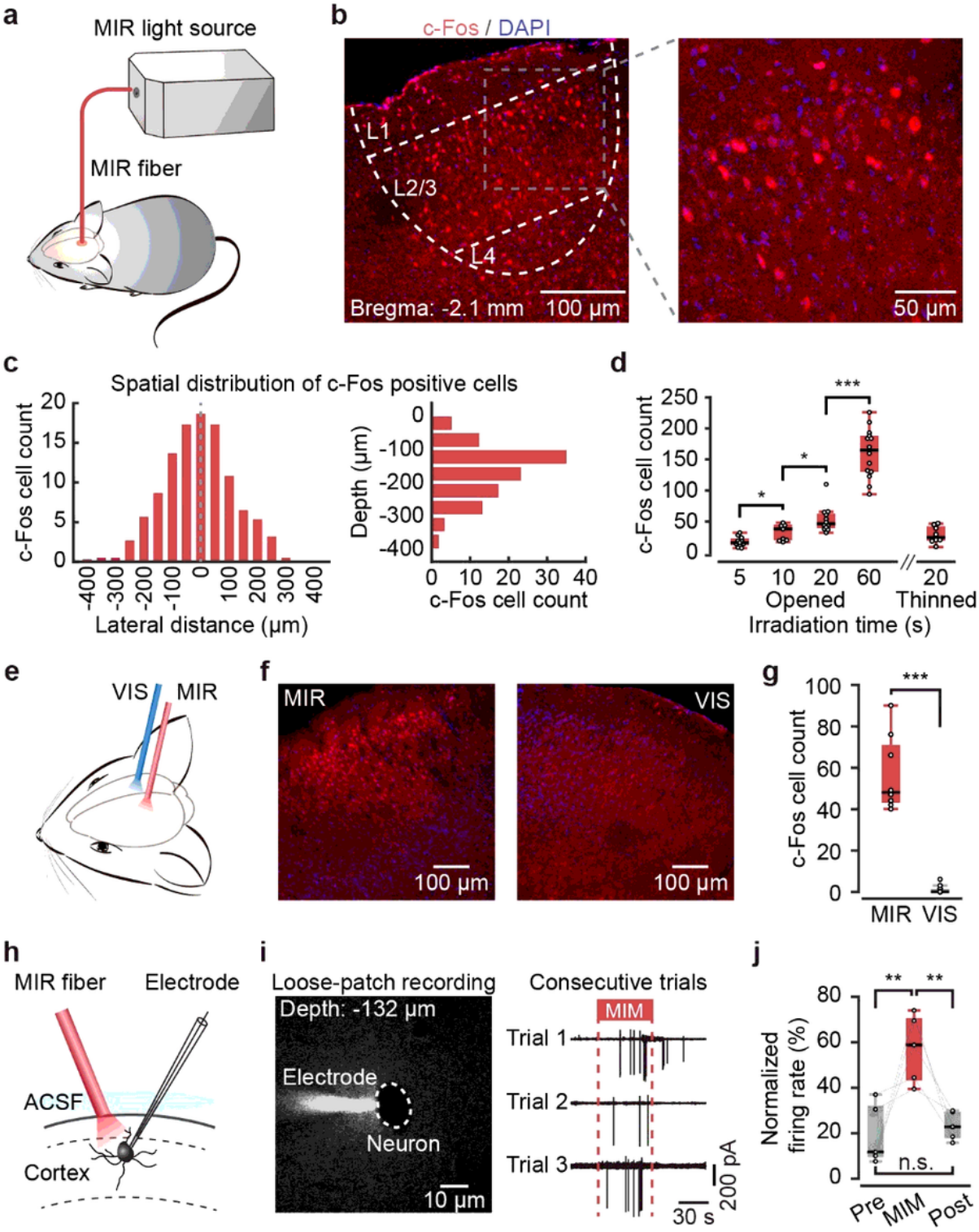

Figure 1

MIM application to the mouse cortex induces neuronal activities. a, General scheme for targeted MIR delivery to mouse brain in vivo. b, Left image: A confocal image of a postmortem slice near the MIR target spot. Right image: magnified view of the left image (gray dashed box). White dashed lines: outlining the cortical layers and the central zone of c-Fos expression, a commonly used marker of neuronal activation. c, Histograms of the lateral (left) and transverse (right) distributions of c-Fos positive cells; datapoints are pooled from 7 animals. See Supplemental Methods for definition of cell counts. d, C-Fos positive cell count in slice samples taken from different groups of mice performed with different MIR irradiation time and conditions (through opened skull or thinned intact skull). Each group consisted of 4 animals. Number of samples in each boxplot as follows: animals with opened skull, '5': 11 slices; '10': 9 slices; '20': 12 slices; '60': 14 slices; animals with thinned skull, '20': 8 slices. e, Schematic showing the MIR-VIS control experimental design. f, Fluorescence images of slices taken at the MIM target spot (left) or the VIS target spot (right), both images taken from the same animal. g, Boxplots showing the c-Fos positive cell count in the MIR- or VIS-exposed regions taken from the same 4 mice (8 slices taken for the MIM group, 11 slices taken for the VIS group). h, Schematic for single-cell loose-patch recording simultaneously with MIM application in vivo. i, Left image: the patch electrode and target cell under live two-photon imaging navigation in vivo. Right traces: 3 consecutive trials of loose-patch recording from one example neuron. j, Boxplots summarizing 5 neurons, showing the normalized firing rate before ('Pre'), during (MIM) and after ('Post') MIM application. Rank sum test, n.s. $p > 0.05$, * $p < 0.05$, ** $p < 0.01$, *** $p < 0.001$, applies for all the relevant figure panels in this study.

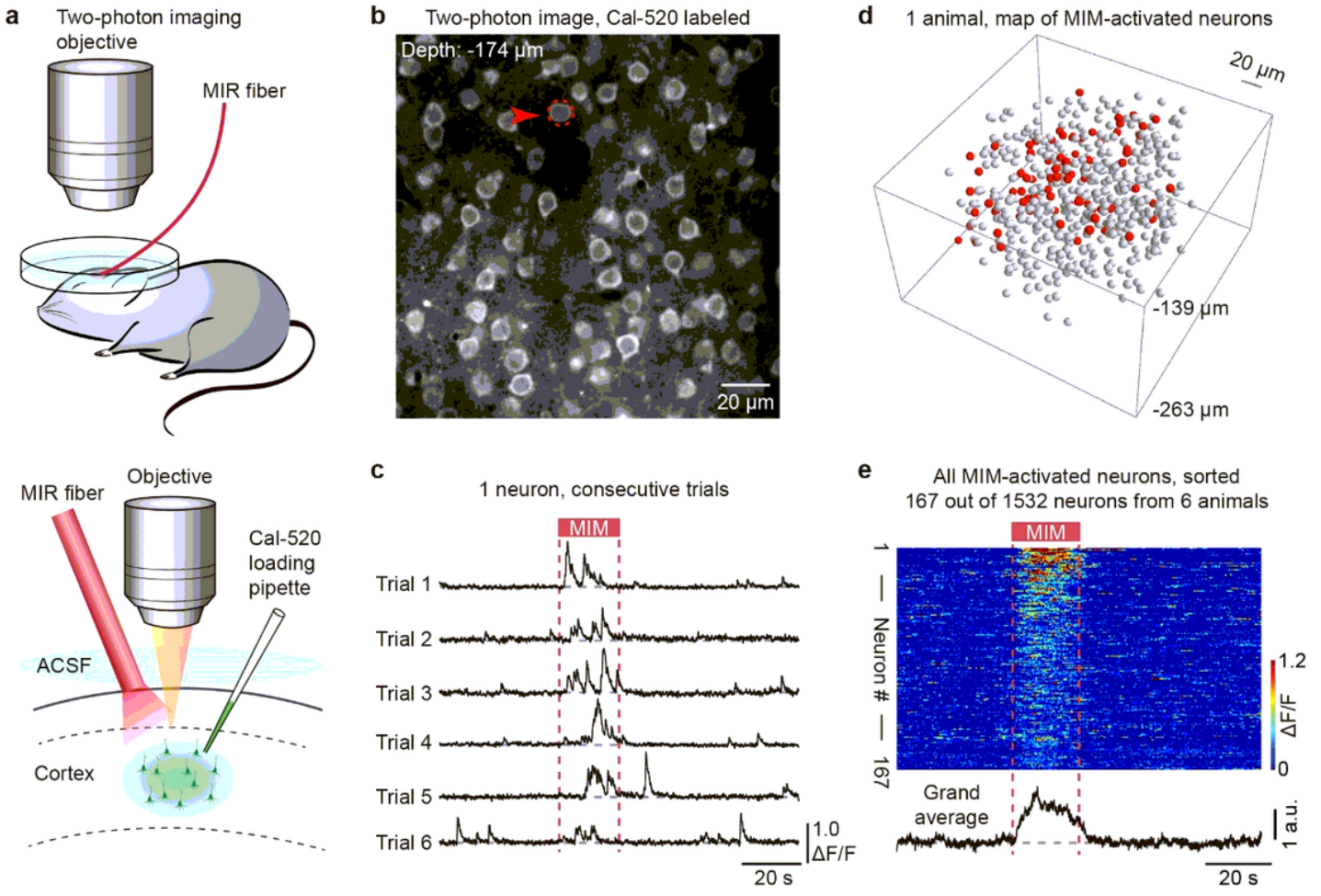

Figure 2

Spatiotemporal mapping of MIM-activated cortical neurons in vivo. a, Upper: cartoon showing the general scheme for the in vivo two-photon imaging experiments. Lower: cartoon showing the configuration of the MIR fiber tip, the two-photon imaging objective and the Ca2+ dye loading micropipette. ACSF: Artificial Cerebrospinal Fluid. b, An example in vivo two-photon image (averaged 100 frames). The red arrow and the dashed circle indicate the neuron for which Ca2+ activity traces are shown in the next panel. c, Ca2+ activity traces of an example neuron (marked in panel b) in 6 consecutive trials. The two red dashed lines indicate the start and the end of the MIM application. d, A reconstructed 3D map showing the positions of all MIM-activated neurons (red balls) and unaffected neurons (gray balls) in the imaged volume, consisting of 8 focal planes from one example mouse. e, Upper: a pseudo-colored plot summarizing the trial-integrated Ca2+ activity trace for each neuron identified as MIM-activated. Neurons were sorted by their relative increment of activity level (from pre-MIM to MIM). Lower: a grand average of the Ca2+ activity traces for all 167 MIM-activated neurons.

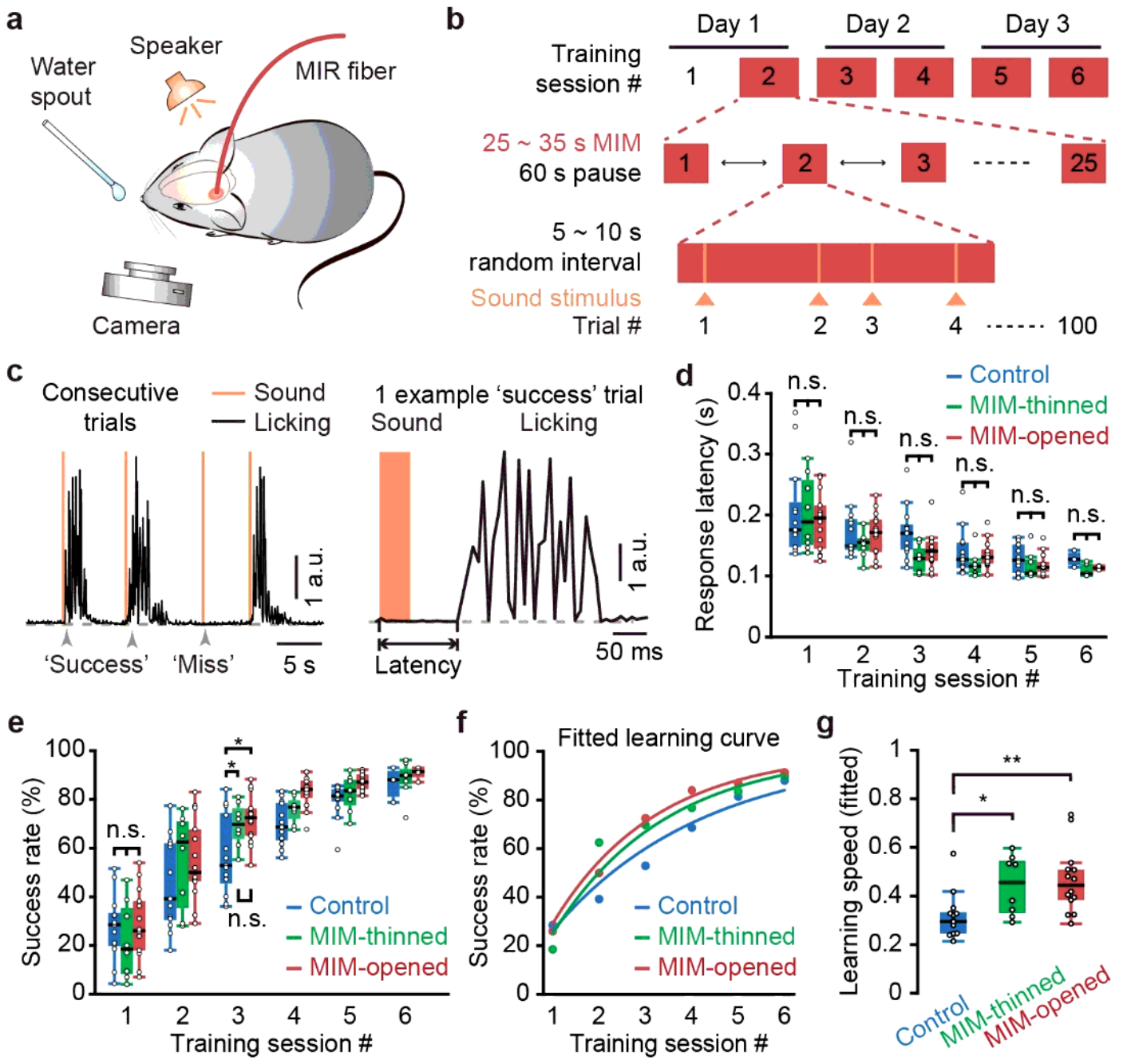

Figure 3

MIM in the auditory cortex accelerates learning during a sound-licking associative training task. a, Schematic illustrating the general scheme for the experiments using MIM in a sound-water associative training task. b, Detail of the experimental protocol for MIM application throughout the training sessions. c, Left trace, an example behavior recording consisting of 4 consecutive trial events, in which the third event was a 'miss' and the other three events were 'success'. Right trace, enlarged view of one successful licking response event to illustrate how the response latency is determined. d, Boxplots showing the latency of licking response for each group in each training session. 'Control': mice with no treatments, 'MIM-opened': mice with MIM applied through a small craniotomy, 'MIM-thinned': mice with MIM applied through thinned intact skull. e, Boxplots showing data for each training session and each group,

representing the success rate for sound-evoked licking response. f, Fitted learning curve for each group, showing the data averaged across the animals in each group respectively. g, Boxplots showing the learning speed inferred from the fitted learning curve. Each data point represents one animal whose learning curve was individually fitted.

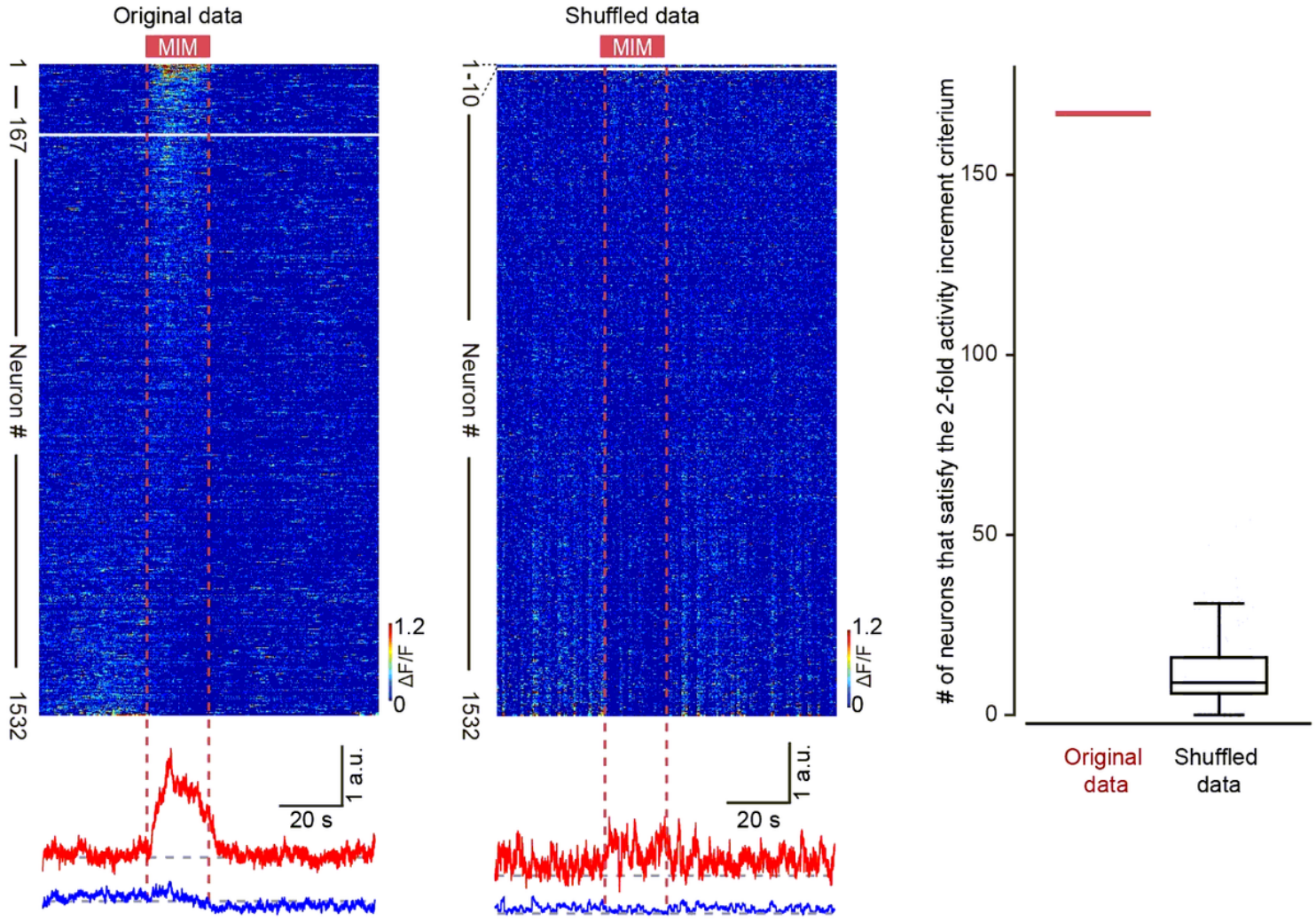

Figure 4

Extended Data Fig. 1 | Complete dataset of the two-photon Ca2+ imaging experiments. Left: Pseudocolored map of trial-averaged Ca2+ activity of altogether 1532 cells which were pooled from recordings in 6 animals, and sorted by their relative increment of Ca2+ activity level from pre-MIM to MIM. The top 167 cells satisfied the '2-fold' criteria that defines a neuron as MIM-activated. Red trace below the map shows the grand average Ca2+ signal trace of the 167 MIM-activated neurons (same as in Fig. 2f), blue trace shows that of the rest 1365 neurons. Middle: The original data were divided into segments of 1 s, and then we randomly assigned the segments of Ca2+ data to shuffle the responses (1000 times). Here only 10 out of 1532 neurons were shown above the 2-fold threshold for the shuffled data. Red trace and blue trace are similar to those in Left panel. Right: The number of MIM-activated neurons for the original data (red) and the shuffled data (black). The number of the MIM-activated neurons was significantly

greater than that of the randomly shuffled data (P = 3.99e-4, two-sided bootstrap test). Boxes represent interquartile range (IQR), central bars indicate the median, and whiskers indicate 1.5× IQR.